Inner-shell photodetachment from Fe^-

I. Dumitriu,[1] R. C. Bilodeau,[1,2] T. W. Gorczyca,[1] C. W. Walter,[3] N. D. Gibson,[3] A. Aguilar,[2] Z. D. Pešić,[1,2,*] D. Rolles,[1,2,†] and N. Berrah[1]

[1]*Department of Physics, Western Michigan University, Kalamazoo, Michigan 49008, USA*

[2]*Advanced Light Source, Lawrence Berkeley National Laboratory, Berkeley, California 94720, USA*

[3]*Department of Physics and Astronomy, Denison University, Granville, Ohio 43023, USA*

(Received 13 December 2009; published 10 May 2010)

Inner-shell photodetachment from Fe^- was studied in the 48- to 72-eV photon energy range using a merged ion-photon-beam technique. The absolute photodetachment cross sections of Fe^-, leading to Fe^+ and Fe^{2+} ion production, were measured. The $3p \rightarrow (3d + \varepsilon d)$ photoexcitation in Fe^- negative ions gives rise to shape resonances. In the near-threshold region, shape-resonance profiles with $l = 2$ accurately fit the single-photodetachment cross section. Simultaneous double photodetachment was also observed, resulting in an increased Fe^{2+} production which obeys a Wannier law. Despite the large number of possible terms resulting from the Fe^- $3d$ open shell, a rough calculation using the R-matrix method qualitatively agrees well with the experimental data.

DOI: 10.1103/PhysRevA.81.053404 PACS number(s): 32.80.Gc, 32.80.Hd

I. INTRODUCTION

Negative ions are a unique class of systems with properties very different from neutral atoms and positive ions. For example, negative ions are extremely sensitive to electron correlation effects [1]. A comprehensive understanding of negative ion spectra could therefore offer a more general understanding of correlated systems, such as certain nanostructures and superconducting materials [2]. Negative ions also play an important role in atmospheric physics, plasma physics, interstellar chemistry, and many other fields [1,3]. Absolute photodetachment cross sections for negative ions are essential for testing the theoretical predictions dealing with many-body effects [4,5] and are needed to model different types of plasmas in astrophysics. Absolute photodetachment cross-section measurements are very challenging and experimental data for negative ions are very limited compared with the data on neutral atoms and positive ions [2].

Throughout the universe, transition $3d$ metals are abundant [6], and the interaction of $3d$ metal atoms and ions with radiation is of great importance for astrophysics. Extensive theoretical work has been performed in order to calculate the photoionization cross sections for atoms and ions of astrophysical relevance (see the Opacity Project [7] or the Ferrum Project [8]). In addition, $3d$ metals and their compounds are of extreme practical importance in metallurgy, magnetism, and data storage systems [9]. The spectra of transition metals are very complex because of the coupling of $3d$ electrons with core holes and strong interaction with the underlying continua [2]. The $3d$ orbital retains, to a high degree, the same characteristics in solids [10], so the atomic and ionic data could be very useful to contribute information toward understanding intra- and interatomic effects.

Iron, lying at the maximum of the nuclear stability curve, is an important astrophysically abundant element [2]. Ionization of iron positive ions by electron impact has been extensively studied in crossed-beam experiments [11]. Several photoionization measurements with synchrotron radiation studying $3p$-photoionization resonances in neutral atomic iron have also been reported [12]. The absolute photoionization cross section of Fe^+ has been measured in a relevant energy region for astrophysical applications (15.8–180 eV) using the merged ion-photon-beam technique [13]. Photoionization of higher charge states of iron has been explored theoretically as part of both the Opacity Project [7] and the Iron Project [14]. However, the accuracies of these calculations are questionable, as shown by a recent systematic photoionization study along the iron isonuclear sequence [15]. Despite numerous research activities for neutral iron and its positive ions, there are only a few valence-shell photodetachment studies for the iron negative ion. The electron affinity of Fe^- [0.151(3) eV [16]] has been determined by laser photoelectron spectroscopy. Measurements of partial photodetachment cross sections and photoelectron angular distributions of Fe^- at visible photon wavelengths have also been reported [17].

The fundamental physics of the interaction of iron atoms and ions with photons is interesting but difficult to analyze in detail. Because of angular momentum coupling there are a large number of possible terms resulting from the open $3d$ shell. Thus, for an accurate description of the photoionization process, strong correlations between these terms as well as relativistic effects have to be taken into account [2,9,10]. The main features in the spectra of the neutral transition metals are the "giant resonances" which appear in the vicinity of the $3p$ threshold [2]. Comparing the resonances in the iron negative-ion photodetachment cross section with the giant resonances in neutral atoms and positive ions will allow detailed insights into the nature of the resonances.

In this work, the photodetachment cross section for Fe^- was obtained by measuring the Fe^+ and Fe^{2+} ion production over the photon energy range 48–72 eV. The absolute cross sections for the production of Fe^+ and Fe^{2+} were measured at four photon energies. Strong shape resonances due to the $3p \rightarrow 3d$

*Present address: Laboratory for Atomic Collision Processes, Institute of Physics, 11080 Belgrade, Serbia.

†Present address: Max Planck Advanced Study Group, Center for Free Electron Laser Science, D-22761 Hamburg, Germany.

photoexcitation were observed above the $3p$ detachment threshold. In addition, simultaneous double photodetachment was also observed, resulting in an increased Fe^{2+} production which obeys a Wannier law.

II. EXPERIMENTAL METHOD

The experiment was performed at the Advanced Light Source (ALS), Lawrence Berkeley National Laboratory, using the High Resolution Atomic Molecular and Optical Physics (HRAMO) undulator beamline 10.0.1 with the ion-photon beamline (IPB), shown in Fig. 1. The IPB endstation [18] uses the merged-beam technique for photoion spectroscopy, where ions and photons travel collinearly in order to increase the interaction volume between photons and the dilute ion beam.

The negative-ion beam with an energy of 8.5 keV was produced using a cesium sputter source (SNICS II from NEC) [19]. The magnetically mass-selected ions were deflected by a 90° spherical electrostatic deflector and merged collinearly with the counterpropagating photon beam. Inner-shell photodetachment from Fe^- followed by Auger decay produced Fe^+ positive ions that were steered out of the primary beam by a 45° demerger magnet and detected as a function of photon energy with an electron multiplier. The demerger magnet also deflected the primary negative-ion beam into a Faraday cup where typical ion currents of 20 nA were recorded after shaping and spatial trimming of the negative-ion beam.

In this apparatus [18], the negative-ion beam with a diameter of 5 mm overlapped the collimated photon beam with a spatial width of 1.2 mm over a distance of about 1.5 m. However, the photon-ion interaction region was defined by a 29.4-cm long stainless-steel cylinder. The 8.5-keV incoming ions were kinetic energy tagged by applying a constant potential of +0.75 kV to the interaction region. The negative Fe^- ions entering in the interaction region were thus accelerated to 9.25 keV, and the positively charged ions Fe^+ (Fe^{2+}) resulting from the photodetachment process exited the interaction region experiencing a second kinetic energy boost of +0.75 keV (+1.50 keV), leaving with 10 keV (10.75 keV) of kinetic energy. The Fe^+ and Fe^{2+} ions formed outside the interaction region, having a lower kinetic energy of 8.5 keV, could then be selected against by the demerger magnet and spherical electrostatic deflector located before the detector. Note that only charged products can be detected with the present apparatus. Therefore neutral Fe atoms, if any, could not be detected.

In order to optimize the ion-photon beam overlap, two rotating wire-beam profile monitors were used at the front and the rear of the interaction region. In addition, the beam was characterized by three translating-slit scanners located near the entrance, middle, and exit of the interaction region. The outputs through these monitors were recorded by a computer and thus two-dimensional (2D) profiles of the ion and photon beams were obtained. The monitors were removed from the beam path during data collection.

The significant background signal produced by collisions between the negative ions and the residual gas ($\sim 4 \times 10^{-10}$ torr) or apertures in the beamline could be accounted for by chopping the photon beam at 6 Hz and subtracting the "photon-off" from the "photon-on" counts. The photon energy was scanned by rotating the spherical-grating monochromator and translating the exit slit of the monochromator while simultaneously adjusting the undulator gap to maximize the photon-beam intensity. Several sweeps over the photon energy of interest were recorded and summed in order to improve the signal-to-noise ratio. The photon energy scale was calibrated using accurately known [2 to 4 meV, uncertainties are quoted to 1 standard deviation (SD) throughout] absorption lines in He [20]. The total uncertainty in the calibrated lab-frame photon energy was estimated to be 40 meV. By direct measurement of the interaction bias potential and the ion-source acceleration potentials, the beam energy in the

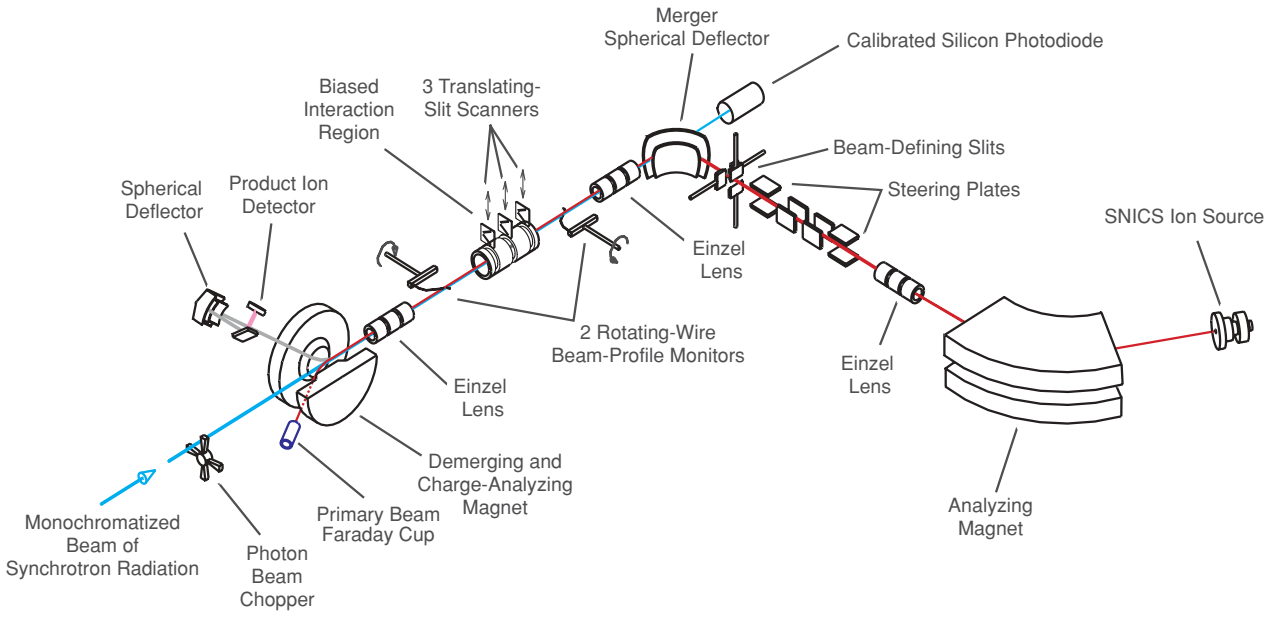

FIG. 1. (Color online) Schematic of photon-ion-beam endstation beamline 10.0.1.

interaction region was determined to be 9.25(17) keV, which gives sufficient ion velocity to produce a significant Doppler shift. In this experiment, the ion-frame Doppler shift is 30 to 42 meV for photon energies of 50 to 70 eV. The energy correction has been applied to all the spectra reported herein.

III. RESULTS AND DISCUSSIONS

The absolute cross sections for photoexcitation of Fe^- leading to Fe^+ production were measured for the four photon energy points listed in Table I. The absolute cross sections σ are calculated from the measurements of the target-ion current I, velocity v, charge q, signal rate R, form factor F, and photon flux Φ as follows: $\sigma = (qvR)/(I\Phi F)$ [18]. The signal rate is $R = R_0/(\Omega_{\rm det}\Omega_{\rm electr})$, where R_0 is the measured count rate, $\Omega_{\rm det}$ is the detector efficiency, and $\Omega_{\rm electr}$ is the pulse detection efficiency of the electronics. In the present experiment, the detector efficiency $\Omega_{\rm det}$ was estimated to be 100(5)% [21] and $\Omega_{\rm electr}$ was 97.5(20)%. Note that we include the possibility of $\Omega_{\rm det} > 100\%$ to account for possible double-counting events arising from electronic ringing and other effects. The total (one standard deviation) systematic instrumental error was $\pm 14\%$.

The 2D form factors $F_z = \int i_x \Phi_x dx \int i_y \Phi_y dy$ were estimated based on ion i and photon Φ beam profiles, which are measured by the slit scanners. The total form factor F, which is a measure of the quality of the overlap of the ion beam with the photon beam, is obtained by integration of the quadratic interpolation of these three 2D form factors over the length of the interaction region. For an accurate determination of the form factor, the ion-photon interaction volume must be well defined. This was accomplished with the +0.750(15) keV applied to the interaction region. The effective interaction-region length of 28.3(14) cm was determined from electrostatic simulations using SIMION 7.00 [22] and the ion kinetic-energy acceptance of the spherical-sector deflectors positioned just before the positive-ion detector.

The ratio of channel strengths (Fe^{2+}:Fe^+) was measured at the same photon energies as the absolute cross sections following the same procedure as previous experiments [23,24]. With the present apparatus, only one channel can be monitored at any particular time. Thus, the signal rates $R(Fe^+)$ and $R(Fe^{2+})$ were recorded in rapid succession (1–4 min per product per energy point) and the measurements were repeated six times to verify that no significant fluctuations in the overlap, ion current, or other such effects were present. The ratio of channel strengths (Fe^{2+}:Fe^+) are reported in Table I. Figure 2 shows the absolute photodetachment cross section of Fe^- to the Fe^+ and Fe^{2+} product channels. The large circles

TABLE I. Measured absolute cross section $Fe^- \rightarrow Fe^+$ and Fe^{2+} and ratio of channel strengths (Fe^{2+}:Fe^+) reported to 1 SD.

Photon energy (eV)	Cross section Fe^+ (Mb)	Cross section Fe^{2+} (Mb)	Ratio of the channel strengths Fe^{2+}:Fe^+
49.23	0.89(13)	0.125(21)	0.141(11)
53.71	5.7(9)	0.59(10)	0.103(8)
58.24	4.5(7)	0.58(10)	0.128(10)
70.24	2.5(4)	0.69(12)	0.275(21)

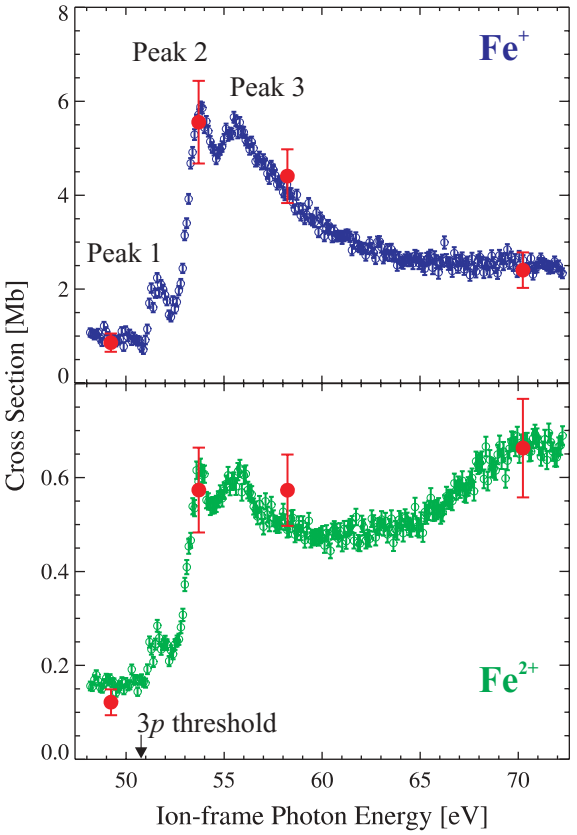

FIG. 2. (Color online) The measured photodetachment cross section for Fe^+ and Fe^{2+} from Fe^-. The cross-section scale was established by making absolute measurements (denoted by filled circles) at the four energies shown.

with error bars in Fig. 2 represent the absolute-cross-section measurements to which the spectra are normalized by using the same method as in previous experiments [18,23,24].

Photodetachment of Fe^- ([Ar] $3d^7 4s^2\,{}^4F_{9/2}$) proceeds from the inner $3p$ shell via three channels. The relevant states in the negative ion, the parent Fe atom, and the positive ion Fe^+ are presented in Fig. 3.

According to dipole-selection rules, the emitted photoelectron can be either an εs or an εd electron (ε represents the kinetic energy of the outgoing electron), and the majority of Fe^+ and Fe^{2+} formation probably happens in step-wise processes that can be written schematically as

$$\begin{aligned} & h\nu + \mathrm{Fe}^-(3p^6 3d^7 4s^2\,{}^4F_{9/2}) \\ & \quad \rightarrow \mathrm{Fe}^{-*}(3p^5 3d^8 4s^2)[{}^4D, {}^4F, {}^4\mathrm{G}] \\ & \quad \downarrow \underline{\text{first step}} \\ & \quad \mathrm{Fe}^{**} + e_{\rm photoelectron} \\ & \quad \downarrow \underline{\text{second step}} \\ & \quad \mathrm{Fe}^{+*} + e_{\rm Auger} \\ & \quad \downarrow \underline{\text{third step}} \\ & \quad \mathrm{Fe}^{2+} + e_{\rm Auger}. \end{aligned} \tag{1}$$

The detachment may also lead to the production of neutral Fe and possibly Fe^{3+}, but neutral Fe cannot be detected with the present system, and no Fe^{3+} ions were observed.

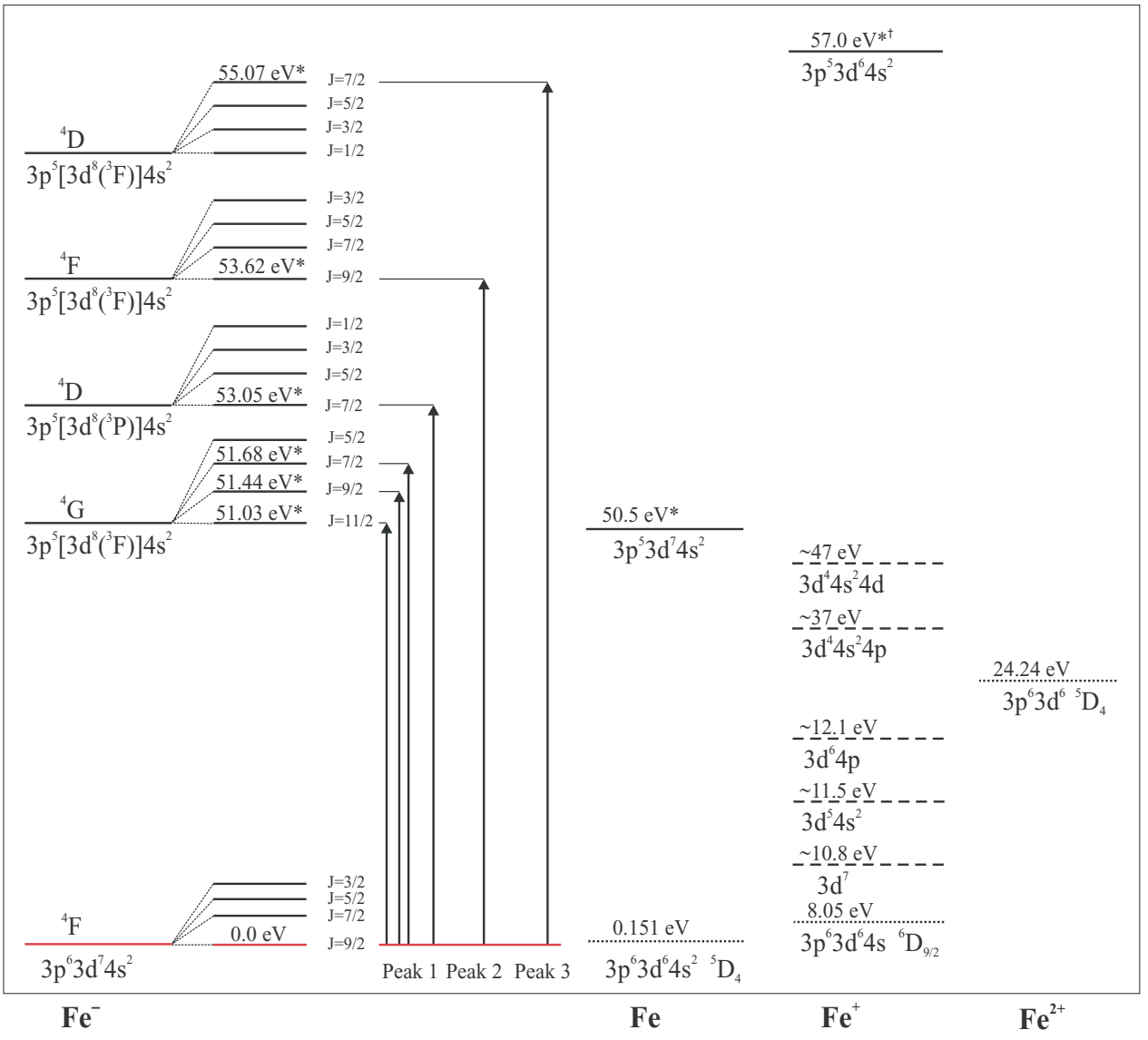

†Theoretical predicted energy for this state is ~66 eV [46].
*State energies measured in the present experiment.

FIG. 3. (Color online) Simplified energy-level diagram for Fe^- and the relevant states in the parent Fe atom and positive ion Fe^+ and Fe^{2+}. For clarity, the diagram is not to scale. The electron affinity of atomic Fe, 0.151(3) eV [16], and all other energies are reported relative to the ground state of the negative ion Fe^-. The solid lines represent the measured state energies. The dotted lines represent the ground state for the Fe [16], Fe^+ and Fe^{2+} [62]. The dashed lines are the theoretically calculated energies of $3p$ excited states of Fe^+ [46].

Excitation of a $3p$ electron in Fe^- leads to quasidiscrete $3p^5 3d^8 4s^2[^4D, ^4F, ^4G]$ shape resonances. In this case, the one-electron potential produced by the short-range attraction and the centrifugal repulsion form a barrier large enough to trap the electron behind it. The primary decay mechanism is tunneling through the barrier, and thus the width and strength of the resonances are influenced by the particular form of the potential. This resonance behavior has been reported for other photodetachment studies such as in Li^- [25–28], B^- [29–31], and C^- [32–34]. In contrast, negative ions for which the valence shell can be filled completely (or become half full) by photoexcitation of an inner-shell electron may exhibit Feshbach resonances due to the enhanced stabilization [23,35,36]. Based on the above studies, and since promoting the $3p$ electron into the $3d$ orbital in Fe^- ($[Ar]3d^7 4s^2\ ^4F_{9/2}$) does not result in filling the subshell, the formation of shape resonances is the most likely. Indeed, three large shape resonances dominate the photodetachment spectrum for Fe^-, leading to Fe^+, as discussed below.

In order to gain a qualitative understanding of the resonance phenomena occurring in the complete photodetachment process, we performed crude calculations using the R-matrix method [37]. Whereas an enormous amount of configuration interaction and a large number of neutral Fe target states would be needed to obtain any type of converged atomic description, and relativistic effects are certainly non-negligible, we were only concerned with the gross features of the photodetachment process so the problem was simplified as follows: First,

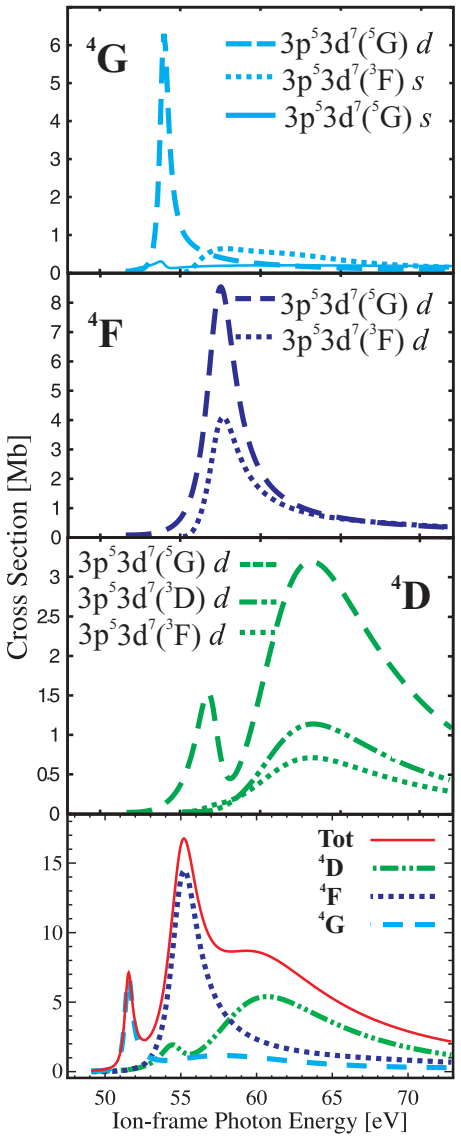

FIG. 4. (Color online) Theoretical results are shown for the individual ^4G, ^4F, and ^4D symmetry contributions (dotted lines) and the total summed cross section (solid line).

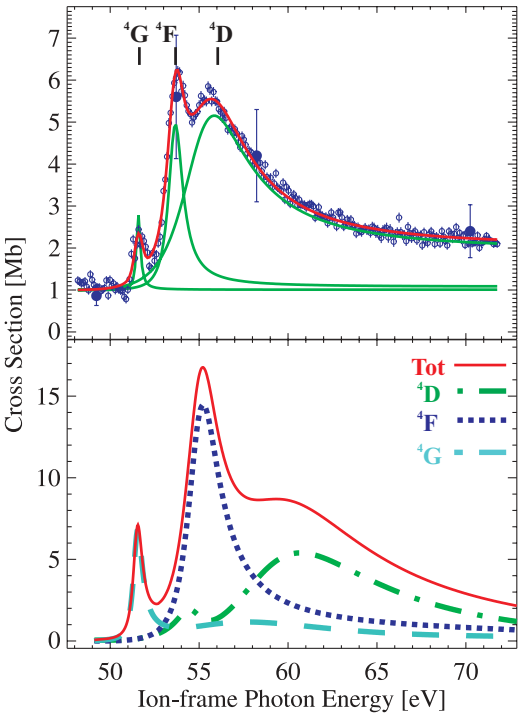

FIG. 5. (Color online) (upper panel) High-resolution (100 meV) cross section of Fe^+ ions following photodetachment of Fe^- [see Equation (1)] over a broad photon energy range. The open circles are the experimental data. The solid lines are the results of three shape-resonance-profile fits to the data. The cross-section scale was established by making absolute measurements (denoted by filled circles) at the four energies shown. (lower panel) Theoretical results were shifted by $\Delta E = -2.4$ eV in order to match the experimental threshold position.

all relativistic effects, including the spin-orbit interaction, were omitted so that an LS description was valid. (We later included relativistic effects in a separate structure calculation, neglecting the continuum, so as to study the fine-structure splitting of resonance states, as mentioned below.) Second, our atomic basis consisted of a single-configuration description for the initial Fe^- $3p^63d^74s^2$ ($^4F_{9/2}$) ground state, the photodetached neutral Fe $3p^63d^64s^2$ ($^5D^e$) ground state, and some of the $3p$-excited Fe* states; namely, the $3p^53d^74s^2$ ($^5G^o$), $3p^53d^74s^2$ ($^5F^o$), $3p^53d^74s^2$ ($^5D^o$), $3p^53d^74s^2$ ($^3G^o$), $3p^53d^74s^2$ ($^3F^o$), and $3p^53d^74s^2$ ($^3D^o$) states. The partial and total theoretical absolute photodetachment cross sections for Fe^- are shown in Fig. 4. By examining the partial cross sections, the dominant contribution in each partial wave is found to be from the $3p^53d^74s^2$ ($^5G^o$) εd channel. This channel gives rise to two ^4D-shape resonances, $3p^5[3d^8(^3P)](^4D)$ and $3p^5[3d^8(^3F)](^4D)$, but only one resonance in each of the other two partial waves $3p^5[3d^8(^3F)](^4F)$ and $3p^5[3d^8(^3F)](^4G)$.

We have assessed that post-collision interaction (PCI) recapture is negligible. As in the earlier cases of B^- [29] and C^- [32] inner-shell photodetachment, even if recapture does occur, only doubly excited Fe** states remain following the departure of the intermediate Auger electron, and these doubly excited states subsequently undergo a second Auger decay, yielding a Fe^+ ion that is detected.

In order to align the photon energies between the experimentally [50.5(5) eV] and theoretically determined thresholds a global shift of −2.4 eV has been applied to the theoretically calculated cross sections (see Fig. 5). The resonance energies and parameters predicted by theory and the measured values are shown in Table II. Since we were unable to include relativistic interactions in our R-matrix calculations, we performed separate multiconfigurational Hartree-Fock (MCHF) structure calculations, where the spin-orbit operator was included, to obtain fine-structure-resolved resonance energies. The resonance widths, on the other hand, were obtained by fitting the R-matrix cross section with shape-resonance profiles. Our crude atomic description of the resonances, using only a single configuration, led to severe overestimates of the resonance energies. Thus, a global shift of −9.4 eV was applied to the theoretical resonance energies in Table II in order to align them with the measured values.

Nevertheless, an overall qualitatively good agreement between theory and experiment can be seen from Fig. 5. We

TABLE II. Details of the resonances.

Resonance		Energy|$_{expt}$ (eV)	Width|$_{expt}$ (eV)	Energy|$_{theor}$[a] (eV)	Width|$_{theor}$[b] (eV)	
$3p^5[3d^8(^3F)]4s^2$	$^4G_{11/2}$	51.21(5)[+]		0.20(4)	51.02	
	$^4G_{9/2}$	51.57(5)[+*]		0.22(6)	51.51	0.63
	$^4G_{7/2}$	51.81(6)[+]		0.47(8)	51.94	
$3p^5[3d^8(^3P)]4s^2$	$^4D_{7/2}$	53.23(6)[+]		0.46(24)	55.22	0.65
$3p^5[3d^8(^3F)]4s^2$	$^4F_{9/2}$	53.62(5)[*]		1.11(9)	56.84	2.25
	$^4F_{7/2}$				57.02	
	$^4D_{7/2}$	55.07(9)[*]		4.32(20)	60.44	8.34

[+]Data shown in Fig. 6.
[*]Data shown in Fig. 5. The $^4F_{9/2}$ and $^4F_{7/2}$ resonances were not resolved in the present experiment.
[a]Present multiconfigurational Hartree-Fock (MCHF) calculation to include fine-structure splitting. The reported theoretical energies are shifted by −9.4 eV in order to match the energy of the $^4G_{11/2}$ state.
[b]Present R-matrix results neglecting spin-orbit splitting.

can attribute the three peaks to $3p \rightarrow (3d + \varepsilon d)$ transitions, with the first sharper structure at about 51.6 eV representing the $3p^6 3d^7 4s^2(^4F_{9/2}) \rightarrow 3p^5 3d^8 4s^2(^4G_{7/2,9/2,11/2})$ excitation, the middle structure at 53.62(5) eV representing the $3p^6 3d^7 4s^2(^4F_{9/2}) \rightarrow 3p^5 3d^8 4s^2(^4F_{7/2,9/2})$ excitation, and the last structure with a long tail at 55.07(9) eV representing the $3p^6 3d^7 4s^2(^4F_{9/2}) \rightarrow 3p^5[3d^8(^3F)]4s^2(^4D_{7/2})$ excitation. The peak widths were found by fitting shape-resonance profiles [38,39] to the resonance peaks giving 1.11(9) and 4.32(20) eV for the second and third peaks, respectively, in Fig. 5 (see Table II). The theoretical fine structure splitting $^4F_{9/2} - {}^4F_{7/2}$ is 174 meV and, given the 1.11(9) eV experimental width of these two peaks combined, the broad natural linewidth does not allow these two resonances to be resolved.

The energy separation of the ^4G and ^4F peaks (first two peaks in Fig. 5) is 2.045(30) eV, slightly lower than the value of 2.78(70) eV determined from the $M_{2,3}$-shell Auger and autoionization spectra of free Fe atoms [40]. Three similar structures shifted at higher photon energy (57.4, 60.6, and 62.7 eV) and with a larger splitting between peaks were observed in isoelectronic neutral atomic Co [41]. The $3p$-photoionization cross section of atomic Fe presents only two broad resonances at 53.5 and 56.2 eV [41]. The absolute photoionization-cross-section data for the positive ion Fe^+ in the $3p \rightarrow 3d$ region [13] and the present data for Fe^- exhibit a strong resemblance. The $Fe^+ \rightarrow Fe^{2+}$ single-photodetachment cross section similarly presents three broad structures around 53.5, 57.0, and 57.5 eV. The $Fe^+ \rightarrow Fe^{3+}$ double-photoionization cross section presents a strong perturbation near the lowest Fe^{2+} $3p^{-1}$ threshold (∼67 eV), showing that the interaction between simultaneous and sequential double photoionization is strong [13].

A. Single photodetachment threshold region

The near-threshold photodetachment cross section of Fe^- was obtained by measuring the positive ion production for Fe^+ in the photon energy range from 50.5 to 53.5 eV with a photon energy resolution of 100 meV and is shown in Fig. 6. Fe^+ production above the $3p$ threshold is dominated by the photodetachment of a single electron followed by further autoionization.

In photodetachment from a negative ion, the near-threshold cross section can be described by the Wigner threshold law [42]: $\sigma \sim (h\nu - \varepsilon_{thr})^{l+1/2}$, where $h\nu$ is the photon energy, ε_{thr} is the threshold energy and l is the angular momentum of the photoelectron. This threshold law has been verified in countless valence-shell detachment experiments [1]. Recent work with $He^-(1s)$, $S^-(2p)$ [23], and $Pt^-(4f)$ [43] has shown that the Wigner threshold law is also valid in inner-shell detachment and p-, s-, and d-wave detachment laws were

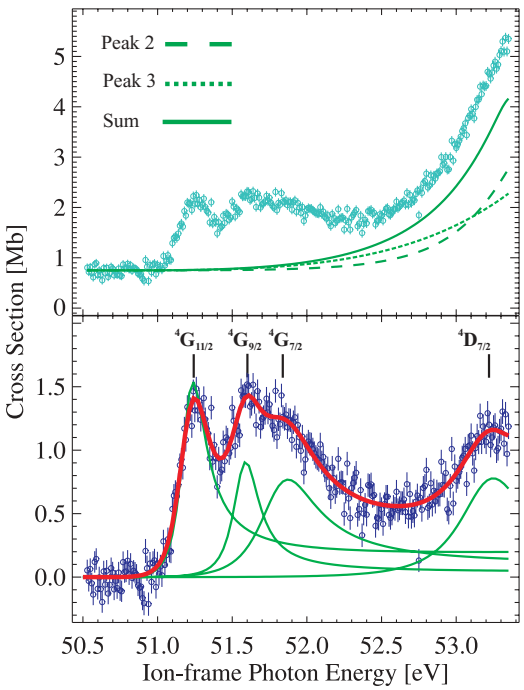

FIG. 6. (Color online) (upper panel) High-resolution (100 meV) cross section of Fe^- leading to Fe^+ over the photon energy range of the first structure shown in Fig. 5. The open circles are the experimental data. Dotted curves are the best fit shape-resonance profiles of the second and third structures in the large photon energy range (see Fig. 5). (lower panel) The same data with this underlying shape-resonance profile from the higher-energy resonances subtracted. The solid lines are the result of four shape-resonance-profile fits to the data.

observed, respectively. However, the presence of a shape resonance near threshold, as in the case of Fe^-, significantly distorts the spectrum. This has been observed in a number of valence studies [38,44,45], and also in inner-shell studies in C^- [32,33] and B^- [29]. In previous studies, it was observed that a modified shape-resonance profile described near-threshold resonances very well in inner-shell processes [29,32,33]. This profile follows that first suggested by Peterson *et al.* [38,39] and successfully used in valence detachment studies. For a shape resonance i near the threshold, we have

$$\sigma^{\text{fit}}(h\nu) = \sigma_0 + A_i \left[\frac{(h\nu - \varepsilon_{\text{thr}})}{(\varepsilon_i - \varepsilon_{\text{thr}})}\right]^{l+\frac{1}{2}} \frac{\Gamma_i/2\pi}{(h\nu - \varepsilon_i)^2 + (\Gamma_i/2)^2}. \tag{2}$$

Here, $h\nu$ is the photon energy, ε_{thr} is the threshold energy, l is the orbital angular momentum of the photoelectron, ε_i is the energy of the resonance, Γ_i is the corresponding natural (Lorentzian) width, σ_0 is the total cross section at the threshold energy, and A_i is the amplitude factor [29]. For the $3p$ photodetachment of Fe^-, the photoelectron can leave with $l = |1_0 \pm 1| = 0$ or 2 (i.e. as an s or a d wave).

The large region of experimental data shown in Fig. 5 was fit using the sum of three modified shape-resonance profiles with $l = 2$ in order to model the observed structures. Results of this fit, which are shown by the solid thin green lines in the top panel of Fig. 5, were then used to model the signal in the $3p$-threshold region. The tails of these two large underlying resonances, represented by the dashed green lines in the top panel of Fig. 6, could be subtracted from the data in order to isolate the resonances in the $3p$-threshold region, as shown in the lower panel of Fig. 6. The resulting near-threshold data was then fit with the sum of shape-resonance profiles ($l = 2$), which reproduce the resonances very well (see lower panel of Fig. 6). The details of the results from the fit are presented in Table II. Note that four shape-resonance profiles are used since, given the initial state $3p^6 3d^7 4s^2(^4F_{9/2})$ and $3p^5 3d^8 4s^2(^4G_{5/2,\ldots,11/2})$ final states, the ΔJ selection rules allow three excitations: $^4F_{9/2} \rightarrow {}^4G_{7/2}$, $^4F_{9/2} \rightarrow {}^4G_{9/2}$, and $^4F_{9/2} \rightarrow {}^4G_{11/2}$. The fourth resonance arises from the $^4F_{9/2} \rightarrow {}^4D_{7/2}(3p^5[3d^8(^3P)]4s^2)$ excitation, and the energy for this resonance is predicted to be about 2-eV higher than the measured value (see Fig. 5). The theoretical calculation predicts the order of the different J states as shown in Fig. 3. The measured splitting of almost all terms is smaller than calculated, see Table III.

B. Simultaneous double-photodetachment threshold

In the present experiment, no distinction can be made between the different final states of the detected Fe^+ or Fe^{2+} ions, and thus the data shown in Fig. 2 represent the sum of all the partial cross sections. Below about 57 eV, the signal for Fe^+ and Fe^{2+} product channels shows no qualitative difference; this is evidence that both charge states in this region are sampling the same process (i.e., the initial $3p$ photodetachment) and are simply formed via different decay routes. However, above 57 eV the Fe^+ production continues to decrease monotonically while that of Fe^{2+} instead increases, indicating some new channel may be opening for Fe^{2+} production, but that is blind to Fe^+ production.

TABLE III. The fine-structure splitting for the resonances.

Term	ΔE_{expt} (eV)	ΔE_{theor} (eV)
$^4G_{11/2} \rightarrow {}^4G_{9/2}$	0.36(7)	0.49
$^4G_{9/2} \rightarrow {}^4G_{7/2}$	0.24(7)	0.42
$^4G_{7/2} \rightarrow {}^4D_{7/2}3p^5[3d^8(^3P)]4s^2$	1.42(8)	0.92
$^4D_{7/2}3p^5[3d^8(^3P)]4s^2 \rightarrow {}^4F_{9/2}$	0.39(7)	1.62
$^4F_{9/2} \rightarrow {}^4F_{7/2}$		0.17
$^4F_{7/2} \rightarrow {}^4D_{7/2}3p^5[3d^8(^3F)]4s^2$	1.45(10)	3.43

*The $^4F_{9/2}$ and $^4F_{7/2}$ resonances were not resolved in the present experiment.

Decay of a Fe^- $3p^{-1}3d^8 4s^2$ shape resonance by autodetachment of the $3d$ electron leaves the system in the Fe $3p^{-1}3d^7 4s^2$ state. Calculations of Fe^+ term energies carried out by Berrington and Ballance [46] have determined the energy levels of interest above the Fe^{2+} limit, which are reproduced in Fig. 3. The main formation of Fe^+ can be explained through simple Auger decay to Fe^+ $3d^5 4s^2$, Fe^+ $3d^6 4s^1$, or Fe^+ $3d^7$. However, these states lie below the Fe^{2+} ground state, so further autodetachment is not possible. Sequential Auger decay cannot produce Fe^{2+}, and production of this ion must proceed through a three-electron process, such as a simultaneous double Auger decay or an Auger-plus-shakeup process populating the higher lying doubly excited states followed by a second autodetachment process. However, simultaneous multielectron photodetachment could also lead to the formation of Fe^{2+}.

Simultaneous double photodetachment is a highly correlated process in which two electrons are simultaneously ejected from the negative ion following the absorption of a single photon. The sequential double-photodetachment process is a two-step process involving the formation of an intermediate core-excited state of the Fe atom which rapidly decays into the two-electron detachment continua, resulting in Fe^+ ions. The reaction can be written as

$$h\nu + \text{Fe}^-(i) \rightarrow \text{Fe}^*(j) + e^-,$$
$$(1) \quad \text{Fe}^*(j) \rightarrow \text{Fe}^{+*}(f) + e^-,$$
$$(2) \quad \text{Fe}^*(j) \rightarrow \text{Fe}^{+^*}(f) + e^- \rightarrow \text{Fe}^{2+*}(f) + e^-,$$
$$(3) \quad \text{Fe}^*(j) \rightarrow \text{Fe}^{2+*}(f) + e^- + e^-.$$

The initial state i is the $3p^6 3d^7 4s^2$ ground state of Fe^-. The intermediate state is an atomic Fe core-excited state [Fe* (j)], mainly $3p^5 3d^7 4s^2$. In general, a core-excited Fe atom may produce neutrals that are not detected in the experiment. As previously mentioned, however, recapture of the photoelectron from PCI effects leaves Fe in an autodetaching state, resulting in the formation of Fe^+, and radiative decay is expected to be insignificant compared with the efficient Auger decay process.

In case (1), the Auger process leaves Fe^+ in the final state f, which is the ground state ($3p^6 3d^6 4s$) or some excited state that does not subsequently autodetach (e.g., $3p^6 3d^7$ or $3p^6 3d^5 4s^2$). Shake-up processes are also possible, in which case other doubly excited states may be formed (e.g., $3d^6 4p$, $3d^5 4s 4p$, $3d^6 4d$, $3d^5 4s 5s$, $3d^5 4s 4d$, etc.). Some of these states may decay into an Fe^{2+} state, which is

depicted by case (2). Finally, case (3) depicts the formation of Fe^{2+} by double Auger decay of the Fe^* state. The measured ratio of Fe^{2+}:Fe^+ production over the photon energy interval 51–57 eV is 9.34(12)% (when the background is correctly accounted for, see below). This is consistent with the range observed in other systems (see, e.g., He^- [47] and S^- [24]). The resonant structures observed in the measured cross sections here are therefore very likely associated with these sequential processes (shape resonances, by their nature, decay by a single-electron tunneling process).

In the simultaneous process, two electrons are simultaneously detached from the Fe^- ion and the reaction can be written as

$$h\nu + \mathrm{Fe}^-(i) \rightarrow \mathrm{Fe}^{+*}(j) + 2e^-,$$
$$\mathrm{Fe}^{+*}(j) \rightarrow \mathrm{Fe}^{2+}(f) + e^-.$$

The initial state i is the $3p^6 3d^7 4s^2$ ground state of Fe^-. The intermediate state j is an excited state of the Fe^+ ion that can decay to either the ground state or an excited final state f of the Fe^{2+} ion.

Usually, the cross section for the sequential process is much larger than the cross section for the simultaneous process [48]. For example, the calculated background double-ionization cross section is up to 10% of the total in Fe^+ and 20% in Fe [46]. Kjeldsen's experiment [13] shows that for Fe^+, double ionization contributes only about 2% of the single-ionization cross section in the $3p \rightarrow d$ region.

To further understand the spectrum, it is of interest to remove the resonant structure from the Fe^{2+} channel in order to more easily see the underlying continuum. Assuming that both the Fe^{2+} and Fe^+ signals are primarily due to the sequential process, as indicated by their very similar cross section (at least below 57 eV), we can use the Fe^+ signal to estimate the simultaneous process in Fe^{2+}. To do this, we first remove the background signal arising from photodetachment to lower-lying states in order to isolate the $3p$-detachment cross section. For Fe^+, this background is almost entirely due to the double photodetachment of valence electrons to the Fe^+ $3d^6 4s$, $3d^7$, and $3d^5 4s^2$ states. A power-law fit to the below-threshold Fe^+ signal returned a power of $-4.3(1.7)$, consistent with the theoretical value for single-electron detachment of -4.5 [49]. A slightly sloped line was sufficient to describe the Fe^{2+} background. The modeled backgrounds (shown in Fig. 7 as dashed lines) were subtracted from the measured Fe^+ and Fe^{2+} data. The resulting Fe^+ signal was then scaled by a factor of 0.0934(12) to match the magnitude of the Fe^{2+} cross section over the photon energy interval (51 to 57 eV) of the resonance. This scaled signal is the estimated sequential-process cross section in Fe^{2+}, and can be subtracted from the total measured Fe^{2+} cross section in order to effectively isolate the signal resulting from double photodetachment (the simultaneous process) with subsequent autodetachment to Fe^{2+}. A clear threshold for this process can be seen in Fig. 7.

In double photodetachment, two electrons emerge from a positively charged ion core. In 1953, Wannier predicted the variation of the double-photoionization cross section with energy in a critical zone where the electron correlation effects dominate [50]. Since then, much effort has gone into testing the Wannier law and its range of validity [51]. There have been

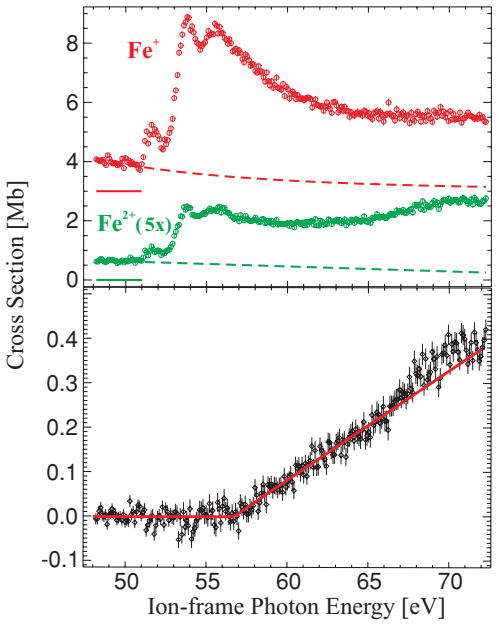

FIG. 7. (Color online) (upper panel) Double-photodetachment cross section $Fe^- \rightarrow Fe^{2+}$. The circles are the experimental data. The dashed lines are the modeled backgrounds. For presentation purposes, the Fe^{2+} signal has been magnified by a factor of 5 here. (lower panel) Simultaneous 2-electron detachment producing Fe^{2+} estimated by assuming that the Fe^+ signal is representative for the single-electron detachment signal. See text for details. The black open diamonds represent the extracted photo-double detachment cross section and the solid red line is the result of power law fits to the extracted photo-double-detachment cross section.

several previous investigations of double-photodetachment cross sections for negative ions such as H^- [52], He^- [5,53,54], Li^- [25,54], K^- [55], Na^- [56], Cl^- [57], and F^- [58].

The near-threshold total cross section for this double-escape process [50,59–61] has the form

$$\sigma_{\mathrm{total}} = \sigma_0 (h\nu - \varepsilon_{\mathrm{thr}})^m,$$

where σ_0 is the total cross section at the threshold energy and $\varepsilon_{\mathrm{thr}}$ is the threshold energy. For the case of double photoionization, m is predicted to be 1.056 [48] and the difference from unity is due to electron-correlation effects.

According to theoretical calculations [46], the Fe^+ states $3d^4 4s^2 4p$, $3d^4 4s^2 4d$, $3d^4 4s^2 5s$, and $3p^5 3d^6 4s^2$ lie above the ground state of the Fe^{2+} ion, as shown in Fig. 3. The formation of the first three excited states in Fe^+ is less likely since it implies correlation effects involving up to four d electrons, while the last one involves only two electrons, a $3p$ and $3d$ electron in a knock-off-type process.

A power-law fit to the extracted double-photodetachment signal returns a threshold position at $\varepsilon_{\mathrm{thr}} = 57.0(6)$ eV and a power of $m = 0.95(20)$, in good agreement with the Wannier threshold law. (This error includes an estimate of our confidence in modeling the background which we determined by repeating the procedure using various reasonable functional forms for the background.) The energy of the $3p^5 3d^6 4s^2$ state was calculated to be ~66 eV [46] above the ground state of the negative Fe^- ion, ~9 eV above the measured Wannier threshold. Considering the difficulty of calculating

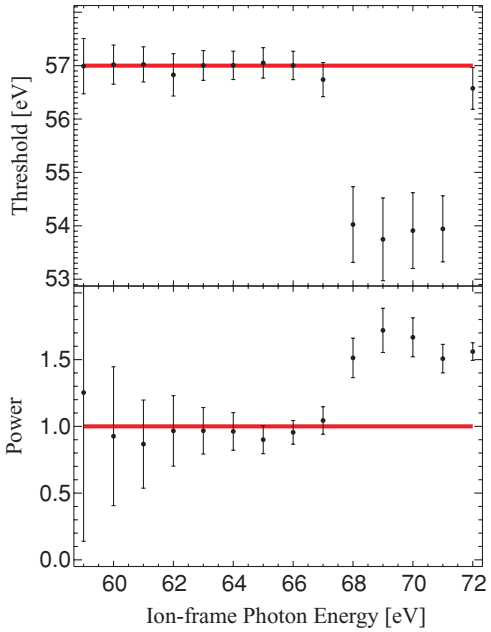

FIG. 8. (Color online) The threshold and power returned by the fit versus the upper limit of the photon energy range used to fit the extracted double-photodetachment cross section. The horizontal red lines are the estimated best values for the Wannier law fit parameters.

this highly excited state in such a complicated system, this overestimation of the energy may be expected, and the threshold in the $Fe^- \rightarrow Fe^{2+}$ photodetachment cross section likely arises from this state. In order to determine its range of validity, we plot the power and the threshold position returned by the fit versus the upper limit of the photon energy range used to fit the data in Fig. 8. A fit of the Wannier law to the near-threshold double-photodetachment extracted signal shows excellent agreement up to 67 eV. The fitted threshold and power values change substantially if photon energies above 67 eV are included in the fit range, due to additional structure in the Fe^{2+} cross section above the Wannier curve over the range 67–72 eV.

IV. CONCLUSIONS

We have reported absolutely scaled inner-shell photodetachment cross-section data for the Fe^- negative ion near and above the $3p$-excitation region. In the photon energy range 48–72 eV, the Fe^- photodetachment spectrum is dominated by shape resonances, which can be assigned to the $3p \rightarrow (3d + \varepsilon d)$ excitation lying just above the $3p$ threshold. In the near-threshold region, the single-photodetachment cross section can be accurately fit using shape-resonance profiles with $l = 2$. The Wannier law was observed and fit well to the near-threshold region of the extracted Fe^- double-photodetachment cross section, observed in the Fe^{2+} production channel. Furthermore, the absolute photodetachment cross sections for Fe^- leading to Fe^+ and Fe^{2+} were measured at four photon energies, providing reference data for astrophysics and plasma physics.

ACKNOWLEDGMENTS

This work was supported by DOE, Office of Science, BES, Chemical, Geoscience and Biological Divisions. The ALS is funded by DOE, Scientific User Facilities Division. N. D. Gibson and C. W. Walter acknowledge support from NSF Grant Nos. 0456916 and 0757976.

[1] T. Andersen, Phys. Rep. **394**, 157 (2004); D. J. Pegg, Nucl. Instrum. Methods B **261**, 138 (2007); M. Ya Amusia, G. F. Gribakin, V. K. Ivanov, and L. V. Chernysheva, J. Phys. B **23**, 385 (1990).

[2] H. Kjeldsen, J. Phys. B **39**, R325 (2006).

[3] J. C. Rienstra-Kiracofe, G. S. Tschumper, H. F. Schaefer, S. Nandi, and G. B. Ellison, Chem. Rev. **102**, 231 (2002).

[4] V. K. Ivanov, J. Phys. B **32**, R67 (1999).

[5] N. Berrah, J. D. Bozek, G. Turri, G. D. Ackerman, B. Rude, H. L. Zhou, and S. T. Manson, Phys. Rev. Lett. **88**, 093001 (2002).

[6] W. Baumjohann and R. A. Treumnann, *Basic Space Plasma Physics* (Imperial College Press, London, 1996).

[7] K. A. Berrington and C. Ballance, J. Phys. B **34**, 2697 (2001).

[8] S. Johansson, A. Derkatch, M. P. Donnelly, H. Hartman, A. Hibbert, H. Karlsson, M. Koch, Z. S. Li, D. S. Lekrone, U. Litzen, H. Lundberg, S. Mannervick, L.-O. Norlin, H. Nilsson, J. Pickering, T. Raassen, D. Rostohar, P. Royen, A. Schmitt, M. Johanning, C. M. Sikström, P. L. Smith, S. Svanberg, and G. M. Wahlgren, Phys. Scr. T **100**, 71 (2002).

[9] M. Martins, K. Godehusen, T. Richter, P. Wernet, and P. Zimmermann, J. Phys. B **39**, R79 (2006).

[10] S. B. Whitfield, R. Wehlitz, and M. Martins, Radiat. Phys. Chem. **70**, 3 (2004); B. Sonntag and P. Zimmermann, Rep. Prog. Phys. **55**, 911 (1992).

[11] M. Stenke, K. Aichele, U. Hartenfeller, D. Hathiramani, M. Steidl, and E. Salzborn, J. Phys. B **32**, 3627 (1999).

[12] C. Gerth, K. Tiedtke, M. Martins, B. Obst, P. Zimmermann, P. Glatzel, A. Verweyen, P. Wernet, and B. Sonntag, J. Phys. B **31**, 2539 (1998); A. von dem Borne *et al.*, Phys. Rev. A **62**, 052703 (2000); K. Tiedtke, C. Gerth, M. Martins, and P. Zimmermann, *ibid.* **64**, 022705 (2001).

[13] H. Kjeldsen, B. Kristensen, F. Folkmann, and T. Andersen, J. Phys. B **35**, 3655 (2002).

[14] S. N. Nahar and A. Pradhan, Astron. Astrophys. Suppl. Ser. **119**, 509 (1996).

[15] M. F. Gharaibeh, Ph.D. thesis, University of Nevada-Reno, 2005.

[16] D. G. Leopold and W. C. Lineberger, J. Chem. Phys. **85**, 51 (1986); T. Andersen, H. K. Haugen, and H. Hotop, J. Phys. Chem. Ref. Data **28**, 1511 (1999).

[17] A. M. Covington, Srividya S. Duvvuri, E. D. Emmons, R. G. Kraus, W. W. Williams, J. S. Thompson, D. Calabrese, D. L. Carpenter, R. D. Collier, T. J. Kvale, and V. T. Davis, Phys. Rev. A **75**, 022711 (2007).

[18] A. M. Covington, A. Aguilar, I. R. Covington, M. F. Gharaibeh, G. Hinojosa, C. A. Shirley, R. A. Phaneuf, I. Alvarez, C. Cisneros, I. Dominguez-Lopez, M. M. Sant'Anna, A. S. Schlachter, B. M. McLaughlin, and A. Dalgarno, Phys. Rev. A **66**, 062710 (2002).

[19] R. Middleton, *A Negative Ion Cookbook* (Department of Physics, University of Pennsylvania, Philadelphia, PA, 1990).
[20] M. Domke, K. Schulz, G. Remmers, G. Kainde, and D. Wintgen, Phys. Rev. A **53**, 1424 (1996).
[21] Based on similar experiments detecting these charged states: R. A. Phaneuf (private communication).
[22] SIMION, Ion and Electron Optics Simulation Software, [http://www.sisweb.com/simion.htm]
[23] R. C. Bilodeau, J. D. Bozek, N. D. Gibson, C. W. Walter, G. D. Ackerman, I. Dumitriu, and N. Berrah, Phys. Rev. Lett. **95**, 083001 (2005).
[24] R. C. Bilodeau, N. D. Gibson, J. D. Bozek, C. W. Walter, G. D. Ackerman, P. Andersson, J. G. Heredia, M. Perri, and N. Berrah, Phys. Rev. A **72**, 050701(R) (2005).
[25] H. Kjeldsen, P. Andersen, F. Folkmann, B. Kristensen, and T. J. Andersen, J. Phys. B **34**, L353 (2001).
[26] N. Berrah, J. D. Bozek, A. A. Wills, G. Turri, H.-L. Zhou, S. T. Manson, G. D. Ackerman, B. Rude, N. D. Gibson, C. W. Walter, L. Vo Ky, A. Hibbert, and S. M. Ferguson, Phys. Rev. Lett. **87**, 253002 (2001).
[27] H.-L. Zhou, S. T. Manson, L. Vo Ky, N. Feautrier, and A. Hibbert, Phys. Rev. Lett. **87**, 023001 (2001).
[28] T. W. Gorczyca, O. Zatsarinny, H.-L. Zhou, S. T. Manson, Z. Felfli, and A. Z. Msezane, Phys. Rev. A **68**, 050703(R) (2003).
[29] N. Berrah, R. C. Bilodeau, I. Dumitriu, J. D. Bozek, N. D. Gibson, C. W. Walter, G. D. Ackerman, O. Zatsarinny, and T. W. Gorczyca, Phys. Rev. A **76**, 032713 (2007).
[30] T. W. Gorczyca, Radiat. Phys. Chem. **70**, 407 (2004).
[31] N. Berrah, R. C. Bilodeau, G. D. Ackerman, J. D. Bozek, G. Turri, E. Kukk, W. T. Cheng, and G. Snell, Radiat. Phys. Chem. **70**, 491 (2004).
[32] C. W. Walter, N. D. Gibson, R. C. Bilodeau, N. Berrah, J. D. Bozek, G. D. Ackerman, and A. Aguilar, Phys. Rev. A **73**, 062702 (2006).
[33] N. D. Gibson, C. W. Walter, O. Zatsarinny, T. W. Gorczyca, G. D. Ackerman, J. D. Bozek, M. Martins, B. M. McLaughlin, and N. Berrah, Phys. Rev. A **67**, 030703(R) (2003).
[34] G. Y. Kashenock and V. K. Ivanov, J. Phys. B **39**, 1379 (2006).
[35] R. C. Bilodeau, J. D. Bozek, A. Aguilar, G. D. Ackerman, G. Turri, and N. Berrah, Phys. Rev. Lett. **93**, 193001 (2004).
[36] H. Kjeldsen, F. Folkmann, T. S. Jacobsen, and J. B. West, Phys. Rev. A **69**, 050501(R) (2004).
[37] P. G. Burke and K. A. Berrington, *Atomic and Molecular Processes: An R-Matrix Approach* (IOP Publishing, Bristol, 1993); K. A. Berrington, W. B. Eissner, and P. N. Norrington, Comput. Phys. Commun. **92**, 290 (1995).
[38] J. R. Peterson, Y. K. Bae, and D. L. Huestis, Phys. Rev. Lett. **55**, 692 (1985).
[39] Y. K. Bae and J. R. Peterson, Phys. Rev. A **32**, 1917 (1985).
[40] E. Schmidt, H. Schroder, B. Sonntag, H. Voss, and H. E. Wetzel, J. Phys. B **17**, 707 (1984).
[41] H. Feist, M. Feldt, Ch. Gerth, M. Martins, P. Sladeczek, and P. Zimmermann, Phys. Rev. A **53**, 760 (1996).
[42] E. P. Wigner, Phys. Rev. **73**, 1002 (1948).
[43] R. C. Bilodeau, I. Dumitriu, N. D. Gibson, C. W. Walter, and N. Berrah, Phys. Rev. A **80**, 031403(R) (2009).
[44] C. W. Walter and J. R. Peterson, Phys. Rev. Lett. **68**, 2281 (1992).
[45] R. C. Bilodeau and H. K. Haugen, Phys. Rev. Lett. **85**, 534 (2000).
[46] K. A. Berrington and C. Ballance, J. Phys. B **34**, L383 (2001).
[47] R. C. Bilodeau, J. D. Bozek, A. Aguilar, G. D. Ackerman, G. Turri, and N. Berrah, Phys. Rev. Lett. **93**, 193001 (2004).
[48] P. Bolognesi, G. C. King, and L. Avaldi, Rad. Phys. Chem. **70**, 207 (2004).
[49] M. Ya. Amusia, N. B. Avdonina, E. G. Drukarev, S. T. Manson, and R. H. Pratt, Phys. Rev. Lett. **85**, 4703 (2000).
[50] G. H. Wannier, Phys. Rev. **90**, 817 (1953).
[51] J. R. Friedman, X. Q. Guo, M. S. Lubell, and M. R. Frankel, Phys. Rev. A **46**, 652 (1992).
[52] J. B. Donahue, P. A. M. Gram, M. V. Hynes, R. W. Hamm, C. A. Frost, H. C. Bryant, K. B. Butterfield, D. A. Clark, and W. W. Smith, Phys. Rev. Lett. **48**, 1538 (1982).
[53] Y. K. Bae, M. J. Coggiola, and J. R. Peterson, Phys. Rev. A **28**, 3378 (1983).
[54] N. Berrah, R. C. Bilodeau, G. D. Ackerman, J. D. Bozek, G. Turri, B. Rude, N. D. Gibson, C. W. Walter, and A. Aguilar, Phys. Scr. T **110**, 51 (2004).
[55] Y. K. Bae and J. R. Peterson, Phys. Rev. A **37**, 3254 (1988).
[56] A. M. Covington, A. Aguilar, V. T. Davis, I. Alvarez, H. C. Bryant, C. Cisneros, M. Halka, D. Hanstorp, G. Hinojosa, A. S. Schlachter, J. S. Thompson, and D. J. Pegg, J. Phys. B **34**, L735 (2001).
[57] A. Aguilar, J. S. Thompson, D. Calabrese, A. M. Covington, C. Cisneros, V. T. Davis, M. S. Gulley, M. Halka, D. Hanstorp, J. Sandström, B. M. McLaughlin, and D. J. Pegg, Phys. Rev. A **69**, 022711 (2004).
[58] V. T. Davis, A. Aguilar, A. M. Covington, J. S. Thompson, D. Calabrese, C. Cisneros, M. S. Gulley, M. Halka, D. Hanstorp, J. Sandström, B. M. McLaughlin, and D. J. Pegg, J. Phys. B **38**, 2579 (2005).
[59] R. Peterkop, J. Phys. B **4**, 513 (1971).
[60] A. R. P. Rau, Phys. Rev. A **4**, 207 (1971)
[61] S. Geltman, *Topics in Atomic Collision Theory* (Krieger, Malabar, Florida, 1969).
[62] Yu. Ralchenko, A. E. Kramida, J. Reader, and NIST ASD Team (2008). NIST Atomic Spectra Database (version 3.1.5), [Online]. Available: [http://physics.nist.gov/asd3] [29 March 2010]. National Institute of Standards and Technology, Gaithersburg, MD.